WIDE-RANGE PRECISION ALIGNMENT FOR THE GEM MUON SYSTEM

Joseph A. Paradiso, David B. Goodwin
Charles Stark Draper Laboratory, Cambridge, Massachusetts, USA

1. GEM MUON ALIGNMENT

The GEM muon system [1] is designed to achieve high momentum resolution by precisely measuring muon trajectories at three equidistant superlayers separated by a long lever arm in a large magnetized volume. In order to retain the desired precision at high momentum (i.e. $\Delta p_t/p_t \approx 5\%$ for the barrel detector at $p_t = 500$ GeV/c), the muon system must determine the net 3-point sagitta of a muon track to $\sigma = 55$ μm in the bending plane. Chamber accuracies, fiducialization placement, alignment transfers, and alignment measurement error are included in this allotment. A set of realizable requirements on these quantities that combine to maintain this 55 μm tolerance are specified in Table 4-1 of Ref. [1], where it has been determined that the false sagitta (i.e. error in the measurement of the bending-plane misalignment of the three superlayers) must be limited to $\sigma = 25$ μm.

Rather than place the drift chamber superlayers with such extreme precision (and require a similar degree of stability from the support structure), the relative positions of the superlayers are actively monitored and the reconstructed spacepoints are correspondingly compensated. A projective alignment scheme that relaxes the chamber positioning requirements in all coordinates has been proposed [2] and simulated [2,3]. Under this scheme, a set of six 3-point straightness monitors are used to measure the superlayer misalignment orthogonal to straight lines that extend along the muon path. Three straightness monitors run from the inner to outer superlayers at opposite edges of a muon alignment "tower" (as depicted in Fig. 2 of Ref. [4]), providing alignment measurements that determine a linear/quadratic interpolation function able to correct alignment-induced false sagitta errors for a projective muon track at arbitrary incidence. This alignment scheme is discussed in more detail elsewhere in these proceedings [4]; its immediate consequence is that the muon superlayers may be placed in the GEM detector relatively coarsely; the current requirements (i.e. Table 1 of Ref. [4]) dictate a placement of ±1 to ±3 mm and ±1 to ±5 milliradians (depending on the superlayer and coordinate), which should be realizable with standard survey techniques (for several practical reasons, it is desirable to avoid highly exacting positioning/stability requirements for structures approaching the size of the GEM muon system, which is 5000 m^3 in volume). Current efforts indicate that it should be possible to extend this range even further by employing an optimal estimator to incorporate other information, such as muon data and sagitta-orthogonal alignment measurements, and improving the θ-coordinate track resolution; the false sagitta then could be appropriately compensated with superlayer misalignments reaching the order of a centimeter.

In conclusion, the GEM muon alignment system requires a precision straightness monitor to be developed that exhibits a resolution better than $\sigma = 25$ μm across a dynamic measurement range approaching a centimeter. This system must perform at this specification in a magnetic field of order 1T and function with an optical path reaching beyond 9 meters (the maximum projective distance between inner and outer superlayers). Since many of these devices are required (i.e. the extreme all-projective alignment system baselined in Ref. [1] requires over 3000 straightness monitors), they must be inexpensive, easy to calibrate/install, and function reliably in the anticipated detector environment.

2. THE VIDEO STRAIGHTNESS MONITOR (VSM) ARCHITECTURE

Three-point optical straightness monitors were first developed [5] for the L3 muon detector at LEP, where they were deployed as the RASNIK [6] system. These are simple devices composed of a light source, lens, and position-sensitive photodetector, as shown in Fig. 1. An image of a smooth-aperture, collimated source (i.e. LED) is projected onto a planar

Presented at the Third International Workshop on Accelerator Alignment, Annecy, France, Sept. 28 - Oct. 1, 1993.

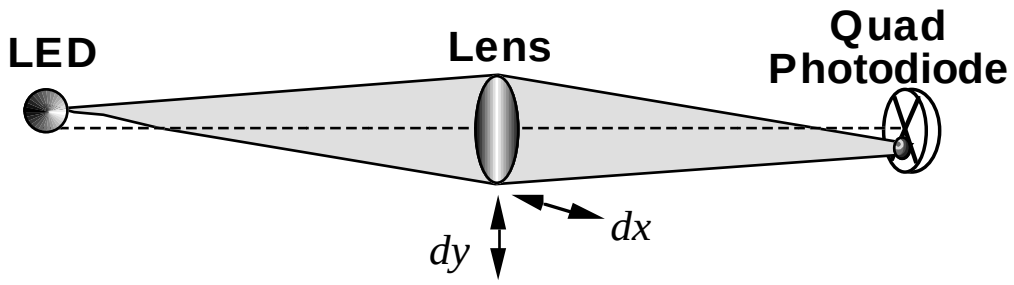

Fig. 1: Standard 3-point straightness monitor as applied in the L3 muon detector

detector (i.e. quadrant photodiode) through a focusing lens. Displacements of the lens from the line between source and detector are measured as a shift in the illumination centroid at the photodiode. With the lens at the midpoint, these devices have an implicit gain of two in the sagitta measurement; the offset read at the detector is twice the 3-point sagitta error. The measured displacement is insensitive to rotations of the lens and LED (provided it exhibits a symmetric illumination profile) about their optical axes. The LED is modulated by a low-frequency carrier, and synchronously detected to minimize the effects of any ambient light background. One straightness monitor component is fixed to each superlayer package such that it precisely references the cathode (sensing) plane of one composite CSC (Cathode Strip Chamber) layer; incident charged tracks (and/or X-rays from a calibration table) will rapidly determine the displacement of the mounted layer (hence the alignment element) with respect to the superlayer mean to better than $\sigma = 10$ μm.

Although simple LED/Lens/Quad-cell systems such as depicted in Fig. 1 are proven to provide high accuracy in deployed detector systems (below 5 μm [6,7]) at minimal cost, their useful measurement range doesn't generally extend beyond 1-2 mm [8]. The range of these alignment systems may be increased by replacing the quad-cell with a continuous lateral-effect photodiode [8] or by employing a wide-area diffuser over the LED and using a larger quadrant diode [9]. These techniques, however, can appreciably increase the hardware complication and expense, plus potentially degrade the alignment resolution beyond the 25 μm limit.

Recent advances in imaging technology and related microelectronics have dramatically reduced the cost and size of solid-state video cameras and image processing hardware. Highly integrated monochrome cameras are now available [10,11] on circuit cards that measure under 45 x 45 mm. They are self-contained, in that they typically require only 12 V of power and will output composite RS-170 video onto a 75 Ω cable. These units are quite inexpensive, costing well below $100 in large quantities. Such cameras typically employ inductive DC/DC converters, however, which prevent operation at high magnetic fields. These converters may be readily bypassed; one of the cameras under investigation [11] has already been so modified for application in the high-field region of a Magnetic Resonance Imager. This technology has an exploding future in many emerging commercial media applications, thus will be aggressively developed, leading to further reductions in price and improved performance.

An early effort [12] in aligning muon chambers focused a single narrow light spot onto a 256-pixel CCD line array, and determined the offset of this feature relative to the sensor by taking the illumination centroid. Because only one feature is detected and a 1D sensor is used, this technique possesses certain drawbacks; the available range is restricted to the active detector area, the measured position can be sensitive to ambient light (thus skewing the centroid), and only one axis of displacement is measured. Now that more powerful 2D video cameras, frame acquisition systems, and processors are available, alignment systems can employ image processing techniques to analyze more complicated, multi-feature images, enabling a robust precision measurement over a much wider range [13].

This concept is illustrated in Fig. 2, where a large precision mask is illuminated and projected through a lens onto a smaller area focal plane array. Misalignment is detected by correlating the captured video image to the mask template. Provided that the portion of the image viewed by the camera is unambiguous, the camera position can be precisely located anywhere across the projected mask, yielding a very wide measurement range.

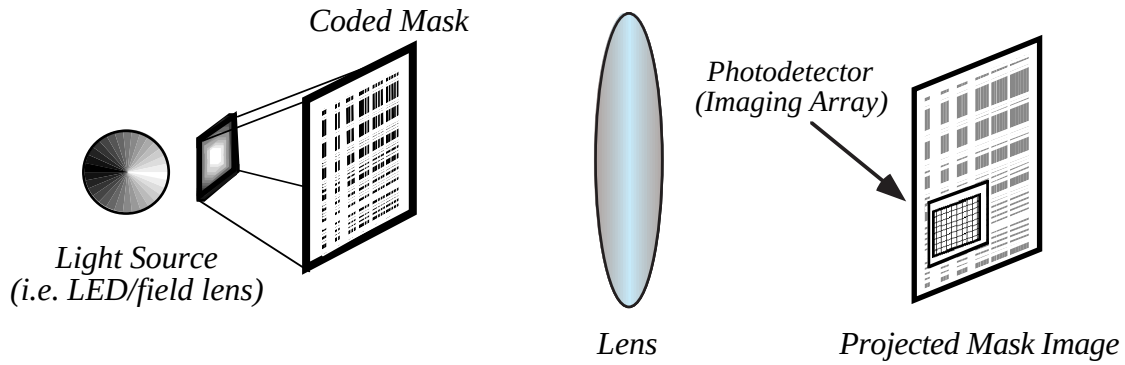

Fig. 2: Video straightness monitor (VSM) scheme

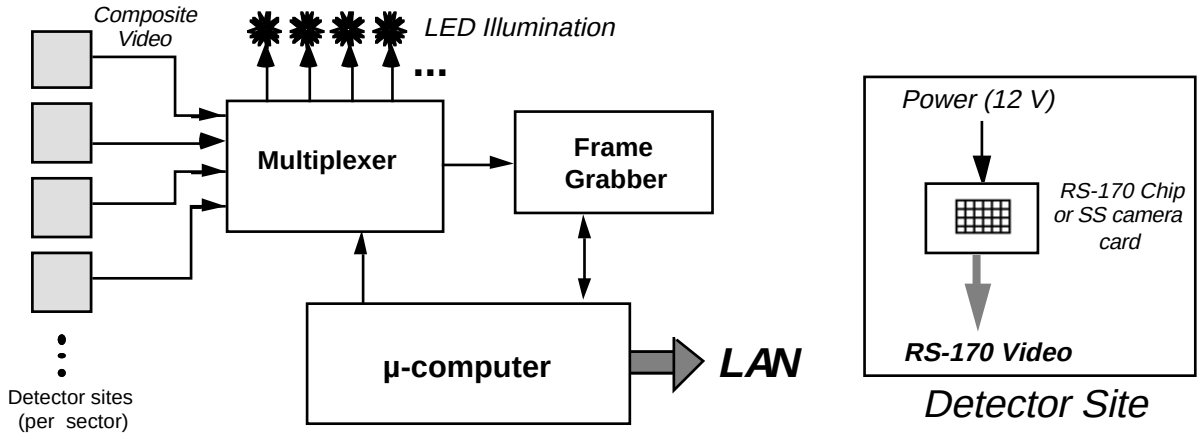

Fig. 3: Data acquisition for multiple-VSM system

Fig. 3 shows the implementation of such a system in the GEM muon detector. This layout entails very little electronics at each monitor site (only an LED illuminator and the camera card), and minimal cabling; a unipolar power supply and video line for the camera (which can both be combined into a single pair), plus a gate for every LED illuminator. Proper shielding will avoid crosstalk into the chamber signal electronics. All video sources for each GEM muon sector (currently estimated to cover $^{1}/_{12}$ of 2π, which includes 136 video channels in the all-projective case [1]) are multiplexed and input to a standard frame-grabber, which is managed by a simple processor that analyzes the captured images as described below and fits to the mask template. Successive frames are summed at a 1 Hz rate for at least 15 seconds in order to average out the effects of atmospheric turbulence. Under these assumptions, the entire muon system can thus be scanned in well under a half hour. The processors will communicate via a Local Area Network, exchanging alignment results, parameters, programs, and diagnostic data. This system is very easy to diagnose and verify; intelligent "watchdog" processing of the video frames provides a wealth of information, and if needed, the real-time video can be visually analyzed.

3. BARCODE DESIGN AND ANALYSIS

The most direct implementation of the VSM technique would be to image a mask of complicated (i.e. pseudorandom) features, and derive the alignment measurement by cross-correlating the captured image to the mask template. This process can be computationally demanding, however, especially if the lens magnification is not precisely known, or there is no coarse *a priori* knowledge of the mask offset. A 2-dimensional barcode has been developed in

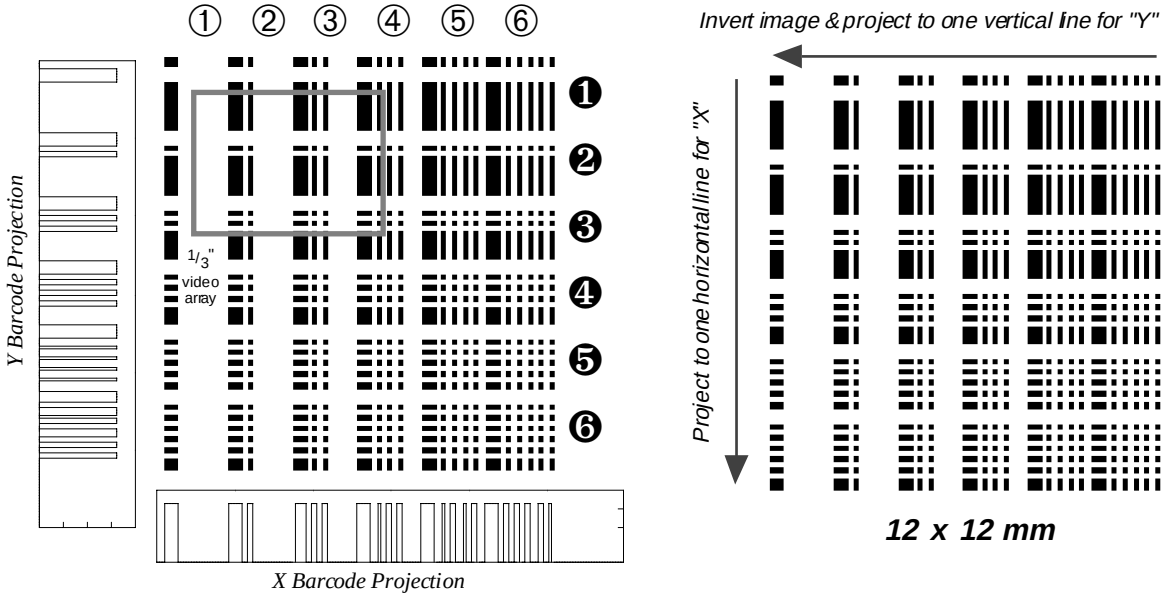

Fig. 4: Principle behind 2-dimensional barcode pattern

order to greatly simplify the needed processing; the two-dimensional pattern matching problem is now decoupled into two essentially independent 1-dimensional problems.

Fig. 4 shows such a barcode and indicates how it is read. The barcode superimposes both x and y information by making one code the negative image of the other. In Fig. 4, we see the horizontal code (x) as being a positive image (black lines), where the vertical code (y) is a negative image (horizontal lines). As indicated at right in Fig. 4, the two barcodes are separated in a captured 2D frame by summing (i.e. "projecting") all pixels horizontally (then reversing their amplitude) for the "y", and summing all pixels vertically for the "x". This yields two 1-dimensional barcodes, as plotted at left in Fig. 4. The barcode digits can be read by simply thresholding this data and counting bars, coarsely positioning the imager relative to the mask (in this simple coding scheme, a thick bar denotes the beginning of a digit; the digit's value is derived by counting the number of narrow bars that follow). Provided that the frame width can accommodate at least two full digits, at least one digit can be completely read at any position, thus the camera offset can be unambiguously determined anywhere in the pattern (every digit in this coding scheme is unique). This is also illustrated at left in Fig. 4, where we see the footprint of a typical $^1/_3$" solid-state imager (such as has been used in tests) superimposed over the barcode pattern. The centroids of the projected bars may then be fit to the code template to produce a precise position reference, as detailed below.

The monotonic barcode of Fig. 4 is extremely simple, and was used in early tests [1]. It was composed manually in a Macintosh drawing package, and the feature locations were extracted into a CAD database. A new barcode has been programmed entirely in PostScript, thus the features are absolutely accurate to the resolution of the output device. This code is shown at left in Fig. 5, and incorporates several additional innovations. The digits are now binary-encoded (i.e. the width of a digit and presence/absence of a bar determines its value), plus the digit sequence is scrambled to insure a more-or-less uniform feature density across the pattern. The thick bars still denote the begin/end of encoded digits. An 8-bar "comb" pattern has been appended to the edges of the main barcode to provide good resolution reaching beyond the edges of the basic code. Because the coding scheme is much more compact, this image is twice as large than that of Fig. 3; the dynamic range is now increased to over 24 mm.

A captured frame (averaged over 15 4-bit grabs) from this barcode is displayed at right in Fig. 5, using the test setup described below. As can be noted, the image is hardly perfect; there are several visible defects due to smudges, etc. on the imager surface and barcode transparency. Because the entire frame is used in analyzing the data, this alignment scheme is tolerant of these defects, and they do not appreciably affect the accuracy. The feature resolution

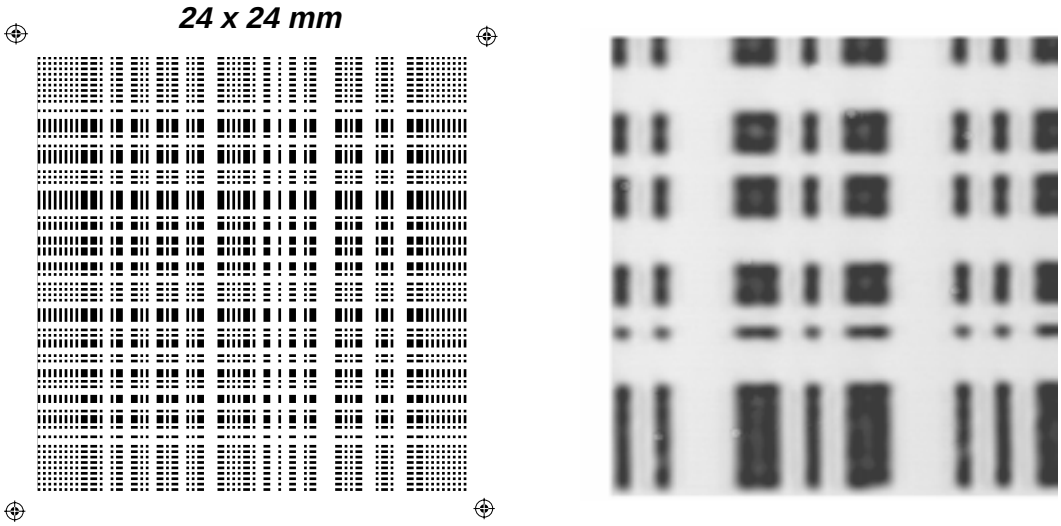

Fig. 5: PostScript barcode (left) and frame captured by test setup (right)

(hence number of possible features, thus length of code and dynamic range) is dictated by the diffraction limit of the lens; in these tests (over an 8 meter path with a 42 mm diameter lens), the narrow-bar features measure ≈120 μm. With the 8 meter baseline, the barcode features are seen to be adequately resolved with a lens aperture down to 25 mm, or defocus of ≈±25 mm (otherwise, the image should be appropriately filtered, etc. before it is analyzed).

An analysis program has been written to process the X\Y projections of frame data; Fig. 6 shows an illustrative plot for a typical projection. First, the data is slightly low-pass filtered (using a phase-invariant Butterworth filter) to remove noise. It is then filtered much more heavily to produce a floating threshold curve, clipped to stay above and below an upper/lower noise floor. The data is discriminated by this threshold to recover the barcode, plotted at the top of the figure. This code is then parsed (i.e. the digits are read and located on the master template), and quadratics are fit to each corresponding peak and narrow valley in order to determine the feature centroids (only data down to half of the peak height is used, to prevent asymmetric tails from skewing the fits; in addition, "valley" data is only used between identical peaks; i.e. between two thick bars or two narrow bars). A linear least-squares fit is then applied to determine the offset and scale factor relating the barcode template reference to the captured frame, as determined by the centroids of the features extracted from the code segments that could be actually read (i.e. those completely in the frame; these are denoted by a "+" in Fig. 6). The remaining features that were detected are then checked to see if they are consistent to within a fiducial tolerance of this fit; if so, the fit is repeated with these points included (the added peaks are tagged "x" and added valleys are tagged "o" in Fig. 6) for greater precision.

The fit performed above relates the imager coordinates (in pixels) from the captured frame to the coordinate system that was used to generate the barcode; i.e. solve for α and β in the relation: $y_{\text{barcode}} = \alpha\, x_{\text{pixels}} + \beta$, where x_{pixels} is a vector of detected feature centroids (in pixels) and y_{barcode} is a vector of the corresponding feature positions in the barcode template (in mm). The current formulation expresses β as the offset of the lower-left corner of the imaging array from the lower left-corner of the barcode; α is the scale factor between the detected and generated barcode. Although the relevant alignment parameter is given by β, fits are performed with both α and β free, which compensates for effects of image magnification and small rotations. If the scale factor α has been calibrated and is stable, it may be held fixed, and only β determined. This produced significant improvement in earlier results [1] with the old manually-generated barcode (Fig. 4), but yields much less benefit with the PostScript barcode of Fig. 5, which has more precise features.

In addition to the above fit technique, another approach was examined, where the barcode template was fit to the entire frame projection (the code was not actually read and no features were extracted) by maximizing the correlation integral and minimizing chi-square.

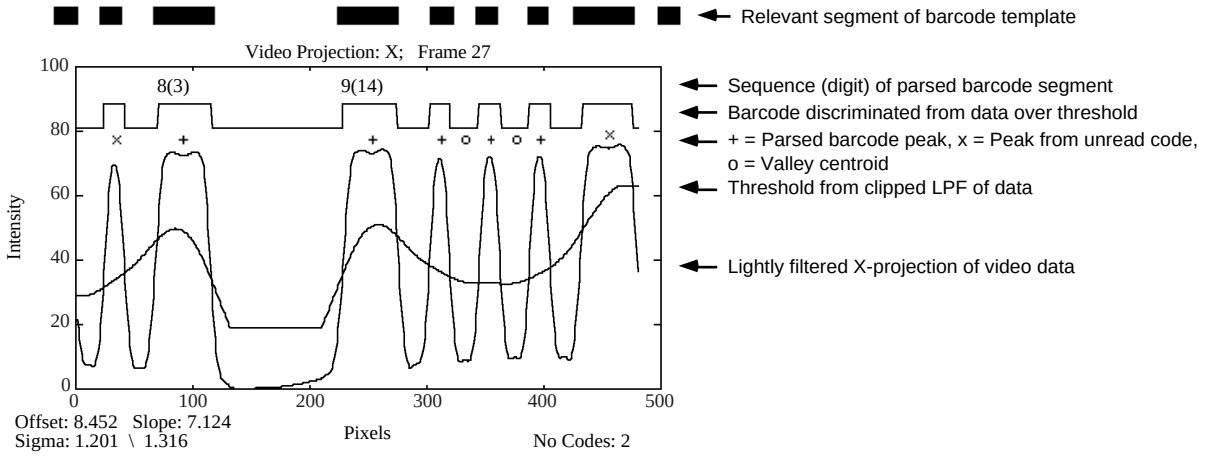

Fig. 6: Analysis of X-projection from captured frame

Because of offset shifts, tails, etc. created by the optical point-spread function, this method produced less accurate results, although the performance may improve after appropriate data filtering. By selecting particular features, such background effects are reduced.

Because of the large amount of data available in the full frame, many effects may be detected and compensated. Rotations of the mask relative to the camera can be determined by performing the feature fit on several band projections across the image (e.g. upper, middle, and lower thirds) or by applying the Hough transform [14] to the 2-dimensional frame data. Small rotational effects in the captured frame may be compensated by translating the calculated β value to the frame center, using the measured scale α.

4. TEST RESULTS

A series of tests was performed on a prototype VSM system. An 8-meter optical baseline (barcode\camera distance) was set up on a 5x12 foot optical table. A 2-meter focal length, 42 mm diameter lens was used at the midpoint to image the barcode at 1:1 magnification. A Chinon CX-102 mini-camera [10] was used, featuring a switched MOS photodiode matrix of 324×246 pixels across a $^1/_3$" diagonal area. Video data was acquired and averaged via a Data Translation DT2861 frame grabber in an IBM PC, and transported to a Macintosh II for analysis, where the above procedure was coded in the MATLAB [15] interpreter. Future efforts [4] will incorporate real-time analysis and will be based entirely around a Macintosh using a SCION LG-3 frame grabber, which can drive a multiplexer and enable up to 64 VSM channels to be addressed.

The PostScript barcode of Fig. 5 was used in these tests. It was printed across a full page using a Linotronic 200 printer with 1200 DPI resolution, and photographically reduced by a factor of 8 (down to 24 x 24 mm) onto a conventional high-contrast negative, which was back-illuminated using a standard IR LED and field lens (which collimates the light like a flashlight beam), as shown in Fig. 2. Future tests [4] will use chrome-on-glass masks made directly from the barcode template, with features accurate to 0.1 μm [16]; the possibility of front-illuminating an opaque mask, which could be lithographed directly onto the cathode plane of a chamber layer, will also be investigated.

In these tests, the lens was translated, and its position computer-monitored by a precision digital linear gauge. The lens displacements are thus quoted in the plots; because of the geometry, the displacement of the source and detector are a factor of two larger.

Results from two scans across the barcode are plotted in Fig. 7. The left column shows the results of a scan across the vertical (Y) axis, and the right column shows the results of a scan across the horizontal (X) axis, as referenced to the barcode drawing in Fig. 5. The top plots show the transfer characteristic; i.e. lens position, measured in mm, vs. the barcode offset (β) as calculated from the fitting procedure described above (both α and β were free in the fits).

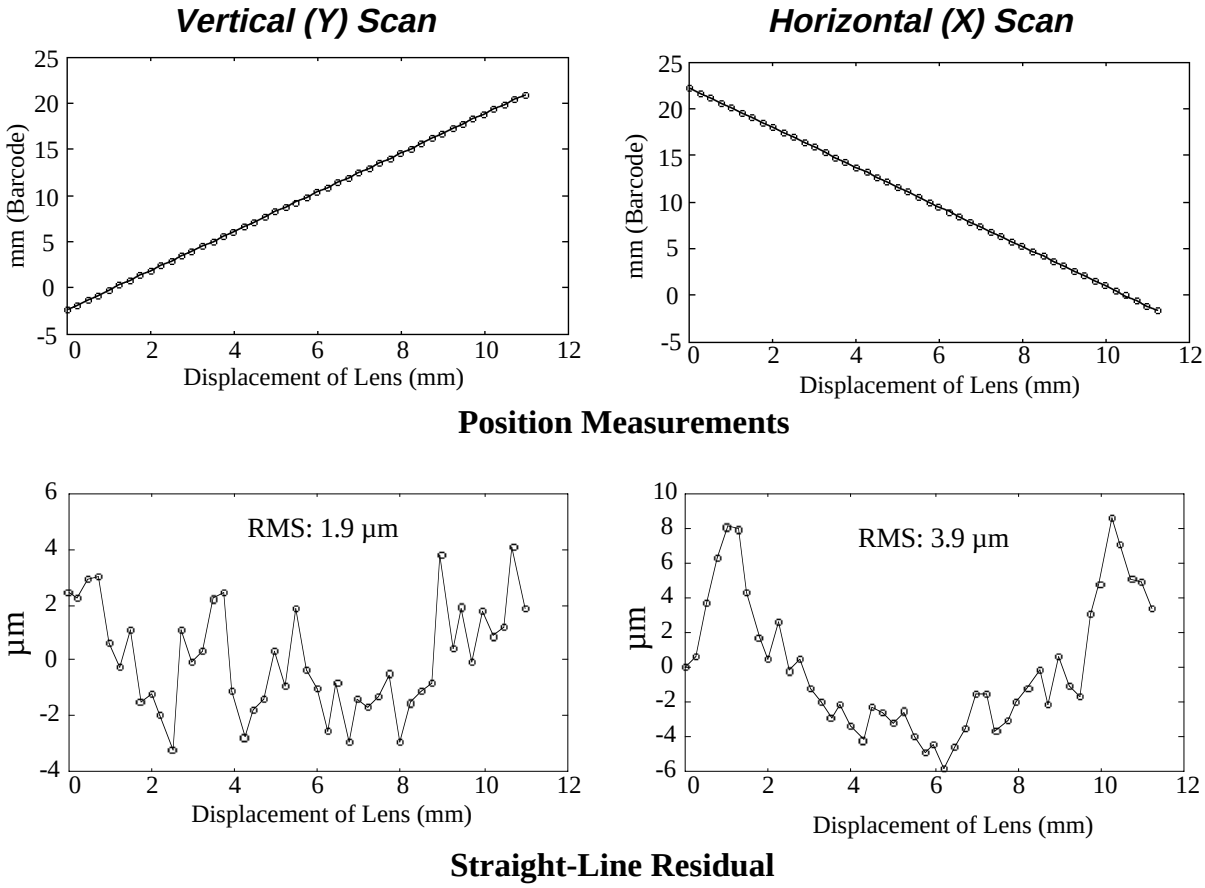

Fig. 7: Transfer characteristic and linearity extracted from VSM scans

The factor of two between lens and detector displacement is obvious from these plots. Because the photographic reduction of the barcode mask was not accurately controlled (thus the template scale is not precisely determined), these plots are essentially calibrations, i.e. they relate the coordinates produced by the barcode fit to the physical displacement of alignment elements (the straight-line sagitta error). The curves are very linear, and span nearly 12 mm of lens displacement (24 mm across the barcode), demonstrating the wide dynamic range.

The lower two plots show the deviation in linearity across these scans. In both cases, the worst-case departures remain below 10 µm. The errors for the vertical scans seem to be mainly due to thermal variations across the 8 meter optical path, and exhibit a σ = 1.9 µm. The horizontal scans show more of a structured nonlinearity (still with RMS under 4 µm), with peaks near either edge of the barcode pattern; nonetheless, these excursions remain within the GEM resolution requirements. In addition, the scan-orthogonal coordinate was resolved for this data (the X coordinate during a Y scan, and vice-versa), to examine the steady-state performance of the system during the test interval (which ran roughly 30 minutes). In both cases, the orthogonal coordinate was stable to within $\sigma < 2$ µm, at which level thermal effects dominate over the 8 meter optical path.

The source of the structured errors seen in the X scan of Fig. 7 is under investigation; possibilities include aberration effects (i.e. narrow-angle illumination during the vertical scan introducing errors when the lens is far off axis) and defects or curl on the mask negative. Another possibility arises from errors generated by wide features – the thick bars yield projections that are not quadratic (see Fig. 6), producing some uncertainty in the resulting centroid fit (due to the rectangular imager aspect, the X scan has a wider scale than the Y scan).

5. CONCLUSIONS AND FUTURE WORK

The video straightness monitors have been demonstrated to resolve sagitta errors to well within 10 μm over long optical path lengths and exhibit over a centimeter of dynamic range in sagitta, as will be required for the GEM muon system. Future efforts will explore effects of image distortion (e.g. recovering from significant turbulence, defocus, etc.), more efficient correlation analysis, extraction of rotational and other information from the 2D data, and establishing efficient fiducialization/calibration procedures [1]. Alternate coding schemes will also be investigated, including multi-digit codes (reading at least two digits at once) for increased range and uni-digit codes (e.g. rather than code several digits separated by thick bars, encode one long digit entirely with narrow bars, in which each captured frame will be uniquely identified); radically different masks have also been suggested [13]. Experience with a multi-channel VSM implementation will be provided by the proposed Alignment Test Stand [4], which will explore the operation of these systems in a realistic environment. The solid-state cameras that will be chosen for GEM must be able to tolerate the anticipated radiation environment. If difficulty is encountered with the candidate devices [10,11], radiation-tolerant imagers using Charge Injection Devices (CIDs) can be employed; if this proves unfeasible, a multiple LED backup option [1] has also been developed.

ACKNOWLEDGMENTS

The authors acknowledge Harry van der Graaf, of NIKHEF, Amsterdam for many discussions that were invaluable to launching this effort, and for several fruitful Internet exchanges since. The optical advice of Jacques Govignon from Draper Laboratory was also appreciated, as were suggestions offered by the GEM muon group, particularly Gena Mitselmakher, Andrey Ostapchuk, Craig Wuest, Frank Taylor, Mike Marx, and Scott Whitaker.

REFERENCES

[1] "GEM Technical Design Report," Chapter 4, GEM-TN-93-262.

[2] Mitselmakher, G. and Ostapchuk, A., GEM-TN-92-202.

[3] Paradiso, J., GEM-TN-92-150.

[4] Wuest, C.R., et. al., these proceedings.

[5] Toth, W. E., Draper Lab Report CSDL-R-1885, Oct. 1987.

[6] Duinker, P., et. al., *Nuc. Inst. and Methods*, A273 (1988), pg. 814-819.

[7] Ayer, F. et. al., *Proc. of the SSCIII Conference, New Orleans LA*, March 1992, p. 151.

[8] Paradiso, J., GEM-TN-92-124.

[9] Post, W., "A Homogeneous Lightsource for RASNIK," NIKHEF-H report, July, 1992.

[10] Chinon CX-103 Solid State Camera, Chinon America, Inc., Mountainside, NJ.

[11] *Electronic Design*, Vol. 41, No. 12, June 10, 1993, pp. 29-32.
See also datasheet on the "Peach" Video camera, VLSI Vision Ltd. Edinburgh, Scotland.

[12] Becker, U. and Paradiso, J., *Nuc. Inst. and Methods*, 196, p. 381 (1982).

[13] van der Graaf, H., personal communication at CERN, Geneva, Fall, 1992.

[14] Gonzalez, R.C. and Woods, R.E., *Digital Image Processing*, Addison-Wesley, Reading, MA., 1992.

[15] MATLAB, Version 3.5, The Math Works, Inc., Natick, MA. 01760.

[16] Photo Sciences Inc., Optical Division, Torrance, CA 90505.